Thermal Unequilibrium of Strained Black $CsPbI_3$ Thin Films

Julian A. Steele,[1]* Handong Jin,[2] Iurii Dovgaliuk,[3] Robert F. Berger,[4] Tom Braeckevelt,[5] Haifeng Yuan,[2,6] Cristina Martin,[7,2] Eduardo Solano,[8] Kurt Lejaeghere,[5] Sven M. J. Rogge,[5] Charlotte Notebaert,[9] Wouter Vandezande,[1] Kris P. F. Janssen,[2] Bart Goderis,[9] Elke Debroye,[2] Ya-Kun Wang,[6] Yitong Dong,[6] Dongxin Ma,[6] Makhsud Saidaminov,[6] Hairen Tan,[6,10] Zhenghong Lu,[11] Vadim Dyadkin,[3] Dmitry Chernyshov,[3] Veronique Van Speybroeck,[5] Edward H. Sargent,[6] Johan Hofkens,[2]* and Maarten B. J. Roeffaers[1]

1) Centre for Surface Chemistry and Catalysis, KU Leuven, Celestijnenlaan 200F, Leuven, 3001, Belgium

2) Department of Chemistry, KU Leuven, Celestijnenlaan 200F, Leuven, 3001, Belgium

3) Swiss-Norwegian Beamlines at the European Synchrotron Radiation Facility, 71 Avenue des Martyrs, F-38000 Grenoble, France

4) Department of Chemistry, Western Washington University, 516 High Street, Bellingham WA 98225, USA

5) Center for Molecular Modeling (CMM), Ghent University, Technologiepark 46, 9052 Zwijnaarde, Belgium

6) Department of Electrical and Computer Engineering, University of Toronto, 35 St George Street, Toronto, Ontario M5S 1A4, Canada

7) Departamento de Química Física, Facultad de Farmacia, Universidad de Castilla-La Mancha, 02071 Albacete, Spain

8) NCD-SWEET beamline, ALBA synchrotron light source, 08290, Cerdanyola del Vallès, Barcelona, Spain

9) Polymer Chemistry and Materials, KU Leuven, Celestijnenlaan 200F, Leuven, 3001, Belgium

10) National Laboratory of Solid State Microstructures, Jiangsu Key Laboratory of Artificial Functional Materials, College of Engineering and Applied Sciences, Nanjing University, Nanjing 210093, China

11) Department of Materials Science and Engineering, University of Toronto, 184 College Street, Toronto, Ontario, M5S 3G4, Canada.

email: julian.steele@kuleuven.be, johan.hofkens@kuleuven.be

Abstract The high-temperature all-inorganic $CsPbI_3$ perovskite black phase is metastable relative to its yellow non-perovskite phase, at room temperature. Since only the black phase is optically active, this represents an impediment for the use of $CsPbI_3$ in optoelectronic devices. We report the use of substrate clamping and biaxial strain to render stable, at room temperature, black phase $CsPbI_3$ thin films. We used synchrotron-based grazing incidence wide angle x-ray scattering to track the introduction of crystal distortions and texture formation within black $CsPbI_3$ thin films when they were cooled following annealing at 330°Celsius. The thermal stability of black $CsPbI_3$ thin films are vastly improved by the strained interface, a response verified by ab initio thermodynamic modelling.

The use of solution-processed organic-inorganic metal halide perovskites for solar cells (*1–5*) is still limited by their instability within real-world devices (*6*), which are twofold. The first relates to the volatility of organic cations in methylammonium (MA) and formamidinium (FA) lead halide systems, which promotes material degradation (*7–9*). The second arises from their polymorphic nature, whereby a room-temperature (RT) stable black perovskite structure is not guaranteed (*10*). Implementing Cs^+ cations (i.e. $CsPbI_3$) has allowed for both high solar cell conversion efficiencies (above 17% (*11*)) and improved environmental stability (*12, 13*). However, regarding phase stability, single-cation FA/$CsPbI_3$ systems form a thermodynamically stable yellow RT δ-phase (non-perovskite) before undergoing reversible high-temperature phase transitions to their optically active black perovskite phases; α (cubic), β (tetragonal) and γ (orthorhombic). The phase diagram for $CsPbI_3$ is depicted in Fig. 1A, with relative transitions and restructuring shown in Fig. 1B. The term "black" is used to define collectively the (pseudo-)cubic phases, as they typically exhibit similar optoelectronic properties. At RT, the black phase is unstable (*14*, *15*).

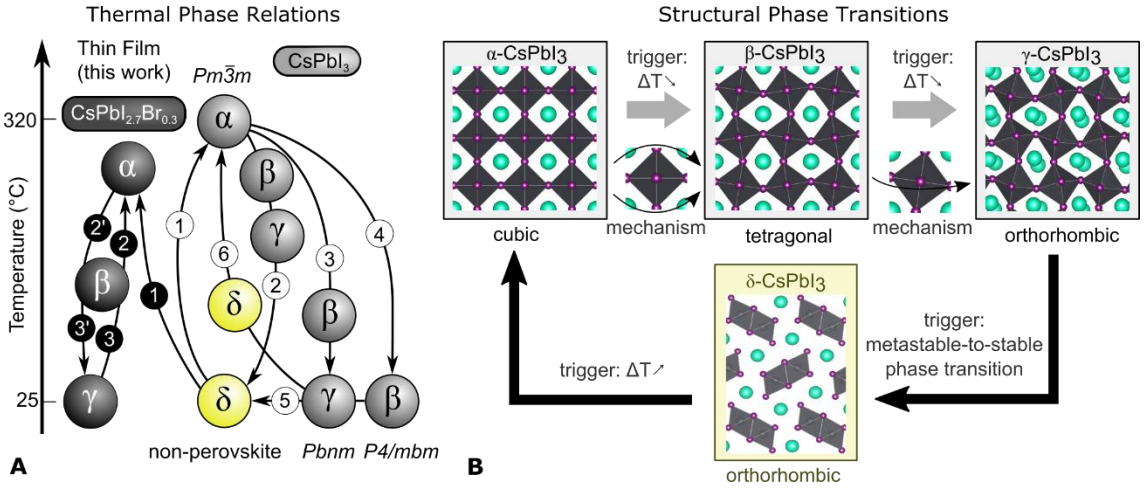

Fig. 1: Polymorphic character and metastability of the $CsPbI_3$ phases. (A) Thermal phase relations of $CsPbI_3$, compared with the phase behavior of strained $CsPbI_{2.7}Br_{0.3}$ thin films investigated in this work. Note the different path details are outline in the text. (B) Crystal structure of the different phases and their relative phase transitions. The transitions between the black phases are governed by the local Pb-centred octahedral (black) distortions, depicted here using one lead atom at the centre and six iodide atoms at the edges (purple), confining the cesium cations (cyan).

As seen in Fig. 1A, the black α-$CsPbI_3$ perovskite can, depending on conditions, pass through a variety of different restructuring paths. The thermodynamically preferred cooling path (path 2) (*16*) is mediated by the series of structural distortions depicted in Figure 1B. When the requisite sample preparation and cooling rates are used, a RT black phase can persist (paths 3 and 4 in Fig. 1A) in the form of a pseudo-cubic phase. A metastable black phase will only survive at RT when a strong driving force to transform into the yellow phase (path 5) is successfully countered. For example, upon mild reheating (60 - 100 °C), the metastable black phase (path 6) will normally turn yellow (*14*, *15*, *17*) once its saddle point is energetically overcome. Thus, the problem is how to form a stable black $CsPbI_3$ perovskite for near-RT device operation.

Recent findings offer a range of solutions, each following at least one of three general approaches: (i) forming nanocrystals (*18–21*), (ii) surface functionalization (*22*), and (iii) compositional tuning (*23–25*). Interestingly, when forming of a perovskite-

substrate heterojunction in thin-film device architectures, tensile strain was recently shown to manifest at RT because of the large mismatch in thermal expansion coefficients (α_T) of the perovskite layer (~50×10^{-6} K^{-1} for lead iodide-based perovskites) and typical optically transparent substrates (both ITO and glass reside between 4×10^{-6} to 9×10^{-6} K^{-1}). By definition, strain will push the competing perovskite phases into a relative state of thermodynamic unequilibrium (*26–28*). Within this context, strain engineering can favor formation of a desired phase or can even lead to new phases (*29*). For example, the strain introduced into $CsPbI_3$ nanocrystals processed with hydroiodic acid (*28*) has been connected to improved stability.

We report the use of interfacial clamping and strain to form a RT stable black phase of functional $CsPbI_3$-based thin films. A combination of synchrotron-based grazing incidence wide angle x-ray scattering (GIWAXS) and ab initio thermodynamic modeling reveal that substrate clamping drives texture formation (preferential alignment of domains within a polycrystalline system) and can create large biaxial strain. Strain beneficially shifted the relative free energies of the competing phases at RT. We elucidate the stabilizing roles of Br doping (≤10%) and thin film formation [i.e. nanocrystal (NC) formation and substrate clamping], and find that strain is a key enabler in the design of stable optoelectronic devices.

We grew $CsPbI_3$ materials using a solution-processing method previously reported (*30*), with the black phase accessed through thermal annealing (see Methods). Three material types were considered: powders (drop cast), thin films (spin coat) and free nanocrystals (NCs) scraped from the thin-film substrate. Figure S1 presents scanning electron microscopy data showing their differing morphologies, where the thin films exhibited the formation of NC grains (50 to 200 nm) and the powders appear bulk-like.

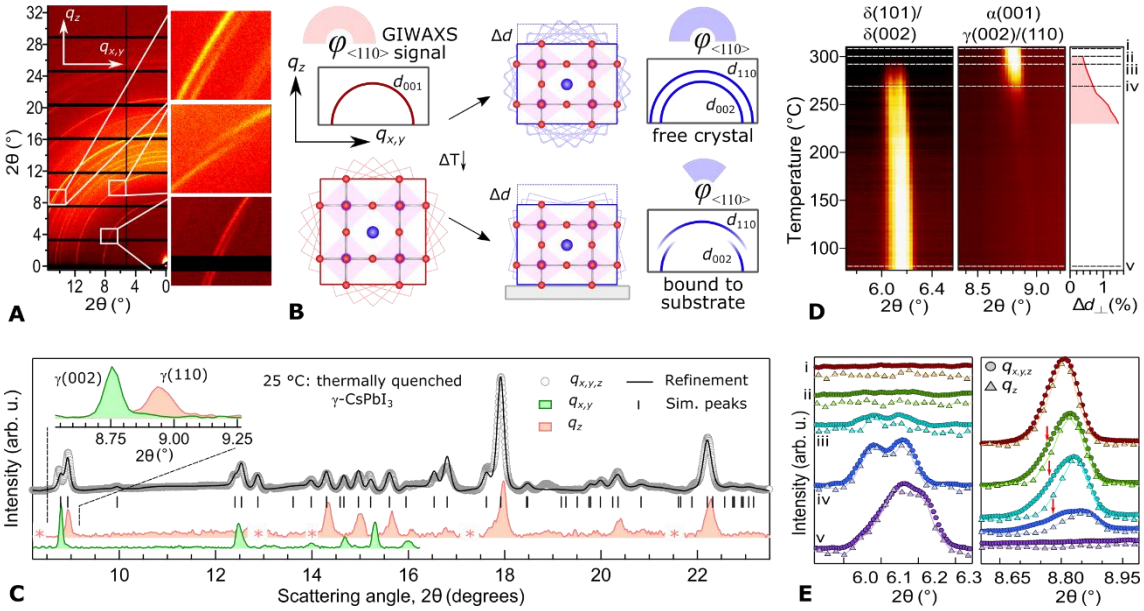

Fig. 2: Structural evaluation of substrate clamping and texture formation following the cooling of high temperature α-CsPbI$_3$ thin films. (A) GIWAXS image acquired from a thermally quenched RT CsPbI$_3$ thin film, with expansions over selected diffraction peaks azimuthally split in the in- ($q_{x,y}$) and out-of-plane (q_z) directions. (B) Schematic illustration of diffraction ring splitting in the GIWAXS signal, whereby a perovskite crystal forms a heterojunction with the substrate surface at high temperatures and undergoes tensile strain and texture formation (with angular distribution φ, represented to light rotated cells) upon cooling. (C) Comparison of GIWAXS 2θ signals generated from the image in (A), formulated by integrating over the total image ($q_{x,y,z}$) and both the $q_{x,y}$ and q_z directions. The "*" symbols indicate scattering blind spots between the cells of the detector and an expansion of the low-angle peaks is inset. (D) GIWAXS *t*-*T* profile and calculated strain $\Delta d_\perp$ (Equ. 1), through an α-to-δ phase transition in a slowly cooled (-5 °C/min) CsPbI$_3$ thin film. (E) Comparison of $q_{x,y,z}$ and q_z 2θ signals extracted at the points marked on the *t*-*T* profile in (D). The arrows identify the missing $q_{x,y}$ signal components detected in the $q_{x,y,z}$ direction, but not the q_z direction.

Synchrotron-based GIWAXS was used (see Fig. S2 for experimental scheme) to resolve the structural state of a CsPbI$_3$ thin film before and during thermal annealing at 330 °C, as well as following thermal quenching (i.e. kinetically trapping the black phase using a RT metal slab; path 3 in Fig. 1A). Figure S3 presents the structural refinements

of a δ-$CsPbI_3$ thin film at RT and its α-phase (330 °C), in line with result of Trots and Myagkota (*31*). A black phase was obtained at RT by kinetically trapping the thin film, hinting toward the role of the interface for suppressing the α-to-δ phase transformation. Figure 2A displays the GIWAXS image detected from a black γ-$CsPbI_3$ thin film shortly after quenching, highlighting occurrences of anisotropic peak splitting in- ($q_{x,y}$) and out- (q_z) of-plane (Fig. S4 shows the full GIWAXS image). This feature is a signature of crystallographic texture (preferential crystallographic orientation with distribution φ; see Fig. S5) in the quenched thin film, a signature not observed before or after gradual cooling (Fig. S6). Figure 2B illustrates how this split GIWAXS signal arises after cooling; the $CsPbI_3$ lattice forming an interface is lengthened in-plane when clamped, corresponding to a relative lattice reduction out-of-plane.

Figure 2C shows analysis of the 2θ scattering intensities generated along directions $q_{x,y}$, q_z and $q_{x,y,z}$. Compared to the cubic α-phase (Fig. S3), a reduction in crystal symmetry is evident from the more complex scattering pattern (*16*, *32*). Refining the $q_{x,y,z}$ data (using Le-Bail method) using a γ-$CsPbI_3$ structure (*16*) provided an agreeable fit and yielded unit cell parameters a=8.629 Å, b=8.955 Å and c= 12.636 Å (vol. = 976.509 $Å^3$). Analyzing the GIWAXS image pixel intensities in Fig. 2A as a function of the azimuthal angle, we are able to quantify the degree of texturing (Fig. S7). We find the intensity of the γ(002)/(020) scattering peaks maximise in-plane, while the γ(200) peak is normal to this and γ(110) exhibits an out-of-plane bi-modal distribution (two maxima separated by ~90°), with full width at half maxima close to 55°, providing a measure of the orientational distribution, φ. An illustration of the crystal texture derived from this analysis is provided in Fig. S8.

The texture was imposed by the symmetry of the initial high-temperature cubic unit cell. Any phase transition that results from a reduction in symmetry (forming an anisotropic cell) is paralleled by the formation of domains, e.g. a transition from a cubic

(α) a to lower symmetry tetragonal phase (β) gives three equally probably domains. In an isotropic bulk α-$CsPbI_3$ system, the domains have the same energy upon cooling and are equally probable. However, the situation changes after the introduction of an anisotropic strain field at the interface that energetically favors some domains, causing the stretched b- and c-axes to remain in-plane (Fig. S7).

Compared with the bulk γ-$CsPbI_3$ structure refined by Marronnier *et al.* (*16*), our thin film γ-$CsPbI_3$ crystal was heavily distorted (Fig. S9) – a result of clamping strain and rapidly cooling the material from 330°C down to RT on a glass substrate. In situ GIWAXS experiments showed that the strained black thin film remains vulnerable to moisture attack, quickly destabilizing and turning yellow when exposed (Fig. S10). In quantifying the extent of crystal deformation, we assessed distortions using the vividly split low-angle peak(s) nearing 2θ = 9°. These peaks arose during the α-to-γ transition through a relative doubling of the *c*-axis [i.e. α(001) becomes γ(002)] and a reduction in the unit cell symmetry, whereby the (110) spacing is no longer equal to (001) in the pseudo-cubic β- or γ-phases. Considering the distortions in- and out-of-plane relative to the parent cubic, we evaluate the degree of biaxial anisotropy as follows:

$$\Delta d_{\perp} = 1 - \frac{d_{(110)}(q_z)}{d_{(001)}(q_{x,y})}. \qquad (1)$$

Here d is the interplane spacing in the direction noted. Because of the relative transformation of the *c*-axis length during the α-to-γ transition, $d_{(001)}$ represents the normalized spacing. For a quenched RT black $CsPbI_3$ thin film; $\Delta d_{\perp}$ = 1.65%.

Two different types of strain act to increase the size of $\Delta d_{\perp}$: (i) spontaneous strain, introduced by a change in unit cell shape during the phase transition(s), and (ii) strain at the film/substrate interface, induced by the thermal expansion mismatch. Spontaneous strain can be decoupled from our measurement by using the temperature-dependent

changes in the bulk $CsPbI_3$ lattice parameters, data recently reported by Marronnier *et al.* (*16*) Analyzing their (*16*) data (see Fig. S8), $\Delta d_\perp$ jumped to 1.18% during the α-to-β tetragonal distortion, and ceased to increase after forming an orthorhombic γ-phase. The value $\Delta d_\perp$ = 1.18% after the tetragonal distortion represents the spontaneous strain contribution of the RT γ-$CsPbI_3$ system, with an additional 0.47% arising in our thin film from substrate clamping. Thus, the effect of the interface is an out-of-plane structural relaxation of the same nature driven by the phase transitions (Fig. 1B), leading to texture formation and a continuation of the spontaneous strain and anisotropy.

To investigate whether the concept of strain induced stabilization was a more general one, we explored the dependence on the thickness of the perovskite thin film. With increasing thickness, the relative volume of the perovskite film that is subject to strain will decrease. The films studied in Fig. 2 are approximately 270 nm thick; so we varied the solution precursor concentration to prepare $CsPbI_3$ thin films with thicknesses ranging from 135 nm up to nearly 1 μm (an upper limit constrained by solubility of precursor) and evaluated the structural state of their kinetically trapped RT black phase using GIWAXS (Fig. S9). The strain profile and texture properties are consistent across the film thickness range studied. Further, $\Delta d_\perp$ retains a value close to 1.65%, though did decrease slightly to 1.62% for the thickest films (Fig. S10). For devices based on solution-processed perovskite thin films, this suggests substrate clamping and the formation biaxial strain to be centrally important.

In a second stage, the properties of the thermodynamically preferred δ-phase material formation were investigated. A slowly cooled $CsPbI_3$ thin film (-5 °C/min) was tracked in situ in Fig. 1D through an α-to-δ phase transition with GIWAXS time-temperature (*t*-*T*) profiling. The black-to-yellow phase change was identified by the introduction of δ peaks near 270 °C and the fading of the black phase peak(s), which turn

asymmetric with reduced crystallographic symmetry. The signals recorded in the $q_{x,y,z}$ and q_z directions are compared in Fig. 2E compares at selected *t*-*T* values in Fig 2D. Again, both strain and texture were established in the black phase during cooling, as seen by the distinct absence of γ(110) scattering in $q_{x,y}$. Before the black phase disappeared, $\Delta d_{\perp}$ increased throughout the phase change toward the expected spontaneous strain limit (~1.2% for purely spontaneous strain; see Figure S9).

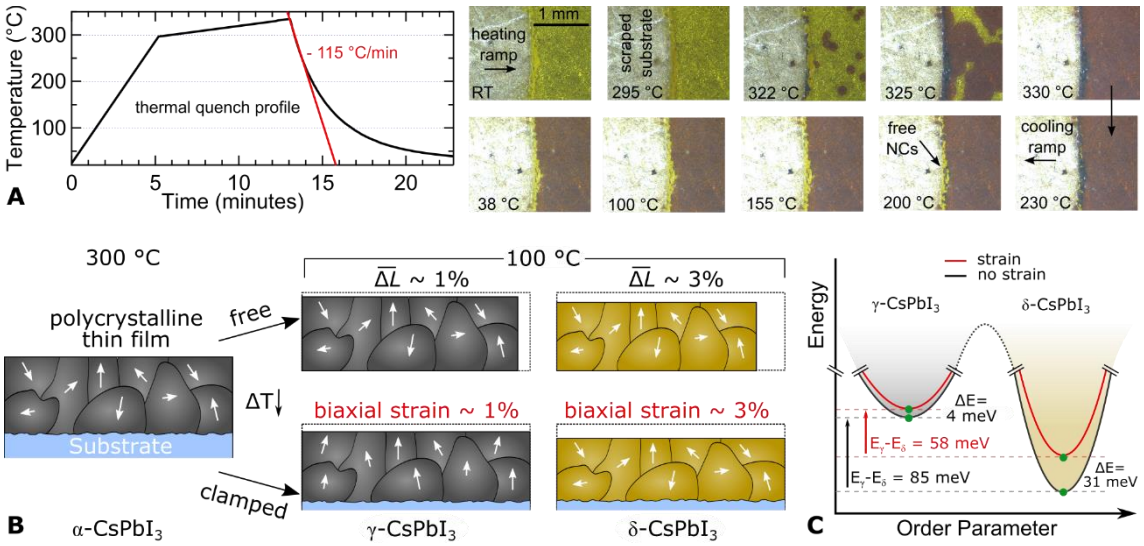

Fig. 3: Removing the interface destabilises RT black $CsPbI_3$ thin films. (A) Corresponding optical images (right) of a partially scrapped $CsPbI_3$ thin film surface (free NCs running down the centre) recorded under N_2 at different temperatures during a quenching temperature profile (left). (B) Schematic representation of the DFT calculations employed to quantify the energy of both the black γ-phase and yellow δ-phase materials that are strongly competing at 100 °C, when cooled from the high-temperature α-$CsPbI_3$. The scenarios considered include both free and clamped polycrystalline thin films (arrows reflecting relative domain orientation), where the thermal change induces a reduction in the average lattice parameter length ($\overline{\Delta L}$), manifesting as biaxial strain when clamped to the substrate. (C) Ab initio energy diagram indicating the relative stability (at 0 K) of the black and yellow phases with and without in-plane biaxial strain, averaged out over 12 different strain directions (see Table S1). Note that the relative saddle point depth is undefined.

The introduction of the yellow phase in Fig. 2E underwent a contrasting evolution; the growth of δ-phase peaks upon cooling was paralleled by the loss of texture and strain within the polycrystalline thin film (Fig. S6). This result indicates that a sharp and clamped interface was lost once transformed to the yellow phase through strain release (i.e. plastic deformation), facilitated by the near-equilibrium transformation kinetics at above 200°C. The constraint of the perovskite atoms at the interface was the cause for this; if the atoms were to remain affixed during a δ-phase restructuring, there would be an increased energy penalty for its formation. The black-to-yellow phase conversion involved a dramatic shift in the crystal volume (*16*) (per unit formula) and a total repositioning of atomic coordinates. The in situ XRD findings of Frolova *et al.* (*15*) visualized this directly, where their [001]-oriented black films (grown by vapor deposition) became disordered after a transition to the yellow phase. They also assigned the results to the large mismatch in the structure of different crystal phase layers relative to the substrate.

To investigate the influence of the strained interface on the relative stability of the α and δ phases, we monitored the local phase of a $CsPbI_3$ thin film that was partly scraped (forming free NCs), as it is thermally quenched from 330 °C (Fig. 3A). From the optical images recorded in situ during the cooling ramp, the material that was still attached to the substrate became kinetically trapped at RT in the black phase, whereas the free NCs readily turned yellow below 230 °C. This result confirmed the stabilizing role of the interface and its generated strain. To check whether the perovskite films respond in a similar way when clamped to other common interfaces, we evaluated the GIWAXS and phase behavior of $CsPbI_3$ thin films deposited on ITO-coated glass substrates (see Fig. S13). The root mean squared (RMS) roughness of the ITO (3.1 nm) is far larger than the bare glass (1.1 nm), yet the strain profile, crystal texture properties and clamping-induced phase properties of thin films on the ITO surface are all comparable (Fig. S13). This extended beneficial substrate clamping across substrates possessing varied roughness and

different chemical natures, suggesting such parameters to be unimportant in establishing a strained interface or a stable black thin film.

To understand the strain-induced shifts in the energetic stability of the competing phases, periodic density functional theory (DFT) calculations of strained and unstrained γ- and δ-$CsPbI_3$ structures were performed (Fig. 2, B and C). Our approach (see Methods) first considered the average unstrained linear reduction ($\overline{\Delta L}$) of the $CsPbI_3$ crystal when it was cooled to 100 °C (where the black and yellow phases strongly compete energetically), which resulted in different degrees of relative contraction for γ and δ (*16*) (Fig. 3B). Our experiments revealed that the interface in the RT black phase prevented shrinking along the in-plane direction, heavily distorting the crystal. As a result, cooling from 300° to 100°C introduced an in-plane biaxial strain of ~ 1%. Our DFT calculations using the SCAN functional (at 0 K) moreover showed that the equilibrium volume per formula unit of δ-$CsPbI_3$ (229 $Å^3$) was substantially less than the γ-$CsPbI_3$ (241 $Å^3$), forcing the strain to grow to ~3% if the material underwent a γ-to-δ phase transition, while remaining clamped. The quenched γ-$CsPbI_3$ thin film was polycrystalline and expressed texture, whereas the crystallographic alignment was lost in the film upon transforming to the yellow phase. To account for this, 12 different crystal orientations were considered, resulting in 12 different strained interfacial planes, with the lower symmetry planes forming supercells (Fig. S14). Their energy increase upon straining is listed in Table S1 and varied only slightly across the different surface orientations.

The average relative energies determined from periodic DFT simulations are shown in Fig. 3C, showing that the unstrained yellow phase is strongly favored over the unstrained black phase; driving the γ-to-δ phase transition in free-standing crystals. However, the introduction of biaxial strain led to different energy penalties for the two phases. Importantly, there was a strong relative destabilization of the strained yellow phase with respect to the strained black phase. Thus, the energy difference promoting the

γ-to-δ transition was reduced, explaining in part the stabilizing influence of substrate clamping we saw experimentally. An additional energy penalty may be present if release of the surface clamping is required, as suggested by the kinetic trapping of the $CsPbI_3$ thin film.

We never formed a RT black phase $CsPbI_3$ thin film without kinetic trapping, such that the limited lifetime of the black phase during relatively slow cooling (Fig. 2D) prevented a detailed study of the strain-induced restructuring. For this, we used relatively light Br halide mixing to better access the temperature-dependent black phase evolution, i.e. $CsPb(I_{1-x}Br_x)_3$, $x \leq 0.1$. Note that these materials retain both a band gap energy useful for solar cells (Figure S15) and comparable material morphologies (Figure S2).

Differential scanning calorimetry (DSC) studies of $CsPb(I_{1-x}Br_x)_3$ powders and NCs (Figure S16) provided two pertinent types of data. First, size-driven effects are likely making the NCs formed during spin coating far more stable than the bulk materials. A disparity in the surface energy between γ-CsPbI3 (0.13 J/m^2) and δ-CsPbI3 (2.57 J/m^2) is predicted (*21*) to reverse the relative magnitudes of their Gibbs free energies at crystal volumes approaching a ~100 nm^3. The size of nanograins making up our thin films (Figure S2) was near this regime. Second, although Br doping helped stabilize the black phase, the calculated enthalpies (Table S2) of the reversible yellow-to-black phase transitions were comparable (13 kJ/mol) and steady across the Br mixing explored. This result suggests that the phase transitions in our mixed halide samples closely followed the thermodynamics of the parent $CsPbI_3$ system.

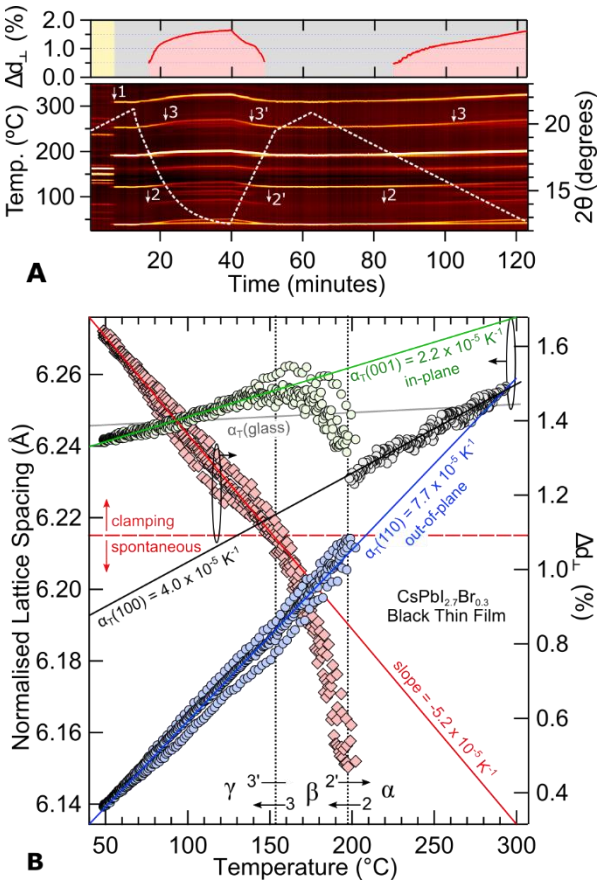

Fig. 4: In situ evaluation of the structural phase kinetics of a strained perovskite thin film. (A) GIWAXS (λ = 0.95774 Å) *t-T* profile ($q_{x,y,z}$) of $CsPbI_{2.7}Br_{0.3}$ thin film through a high-temperature yellow to black phase transition, followed by thermal cycling. The start of the first cooling ramp (non-linear) is roughly -17 °C/min and the second is -3.8 °C/min. (B) Normalized anisotropic lattice parameters and out-of-plane distortions $\Delta d_{\perp}$ of the black phase thin film, as a function of temperature. Phase changes are numerically identified in (B) and align with those depicted in (A). The linear fits to selected segments generate the α_T values displayed. An estimate is provided for the thermal expansion of the glass substrate (*33*) (α_T=0.37×10^{-5} K^{-1}).

Figure 4A shows the GIWAXS *t-T* profile and strain state in a $CsPbI_{2.7}Br_{0.3}$ thin film through multiple phase transitions imposed during thermal cycling. The changes therein can be tracked following the successive phase transitions, whereas the emergence of texture induced by anisotropic strain results in azimuthal splitting; the latter effect can only be seen with a large area detector. Starting from δ-$CsPbI_{2.7}Br_{0.3}$, we saw the high-

temperature formation of the α-phase (1), followed by β (2) and γ (3) distortion during cooling, which were reversed (2' and 3') upon reheating. After an initial yellow-to-black transition, a thermodynamically stable black thin film with a strained interface is realised thereafter. This contrasts the unstable free NCs explored via DSC in Fig. S16, which do not benefit from the stabilizing strained interface. For completeness, the sequence described above for thin film $CsPbI_{2.7}Br_{0.3}$ is compared to the nominal thermal phase relations of $CsPbI_3$ in Fig. 1A. The textured GIWAXS signal (raw image in Fig. S17) and the crystal structure of the RT γ-$CsPbI_{2.7}Br_{0.3}$ thin film is analogous to the quenched black $CsPbI_3$ thin film (Fig. S4). The magnitude of $\Delta d_{\perp}$ in the γ-$CsPbI_{2.7}Br_{0.3}$ thin film at RT reached 1.64% and reheating caused the strain-driven texture to be undone, reforming randomly distributed α-phase domains (see Figure S18). Thus, besides hindering a decay to the δ-phase (Fig. S16), kinetically trapping a black $CsPbI_3$ thin film incurred no additional structural modification.

A temperature-domain structural analysis of the black $CsPbI_{2.7}Br_{0.3}$ thin film (Fig. 4B) showed no considerable hysteresis between the different restructuring pathways (Figure S19). We thus evaluate these data together; as the temperature difference (ΔT) increased, the interplanar distances d shifted relative to $d_0(\Delta T = 0)$ by: $d = d_0(1 + \alpha_T \times \Delta T)$. Linear fits yielded the α_T values (Fig. 4B) using high-temperature d_0 values. Upon cooling the black film from 300°C, the lattice *a*-axis contracted smoothly with an expansion rate comparable (*31*) to the high temperature α-$CsPbI_3$ ($\alpha_T = 4.0 \times 10^{-5}$ K^{-1}). Near 200°C the cubic structure underwent a tetragonal distortion and the introduction of $\Delta d_{\perp}$ through spontaneous strain formation. The in-plane (001) lattice underwent negative thermal expansion, reverting this in-plane lattice closer to the linear expansion rate of glass. The negative thermal expansion of the *c*-axis in this temperature range agreed well with the complex bulk structural evolution detailed by Marronnier *et al.* (*16*) (see Figure S9 for full analysis), and underpinned the subsequent texture direction. Cooling through point 3 in Fig. 4B, the out-of-plane lattice continued its relatively fast reduction, whereas the in-

plane spacing of the orthorhombic structure assumed positive thermal expansion [compensated by negative thermal expansion of the *b*-axis (*16*); see Figure S9]. After the β-to-γ transition, $\Delta d_{\perp}$ should not increase in a non-strained system. In our clamped thin film $\Delta d_{\perp}$ grew rapidly and overshot spontaneous strain contributions, being driven solely by the strained interface. With rising strain, the relative destabilization of the yellow phase was only expected to continue.

The small divergence of the in-plane $CsPbI_3$ lattice parameter (crystal *c*-axis) from the expected linear contraction of the glass suggests that the perovskite/substrate interface resulted from the adaptable nature of the perovskite crystal, rather than covalent bonding. This is also supported by our studies of strained films deposited on ITO-covered glass (S13). The strong mirroring of the structural evolutions during thermal cycling signified high elastic recovery. Together, clamping and interfacial strain combined as key driving forces in defining both the structural texture and the improved thermal phase relations of the black phase. Thus, once a δ-$CsPbI_{2.7}Br_{0.3}$ thin film was annealed at high temperatures, it became thermodynamically trapped in an optically-active black phase (Fig. 1A). Such thermal stability is highly desirable within optoelectronic devices; for instance, the energy provided by an LED driving current can readily destabilize the black phase (*34*). As a conceptual demonstrator, we fabricated and characterised a functioning LED device using a strained $CsPbI_{2.7}Br_{0.3}$ active layer (see Figure S20 for full details). Without any optimization, the result is a working LED device with a visibly bright (luminance of 20 cd/m^2 at 9 V) and high color purity (CIE coordinates: 0.72, 0.28) emission.

References and notes

1. M. A. Green, A. Ho-Baillie, H. J. Snaith, The emergence of perovskite solar cells. *Nat Photon*. **8**, 506–514 (2014).

2. P. Meredith, A. Armin, Scaling of next generation solution processed organic and perovskite solar cells. *Nature Communications*. **9**, 5261 (2018).

3. S. D. Stranks *et al.*, Electron-Hole Diffusion Lengths Exceeding 1 Micrometer in an Organometal Trihalide Perovskite Absorber. *Science*. **342**, 341–344 (2013).

4. A. Walsh, A. Zunger, Instilling defect tolerance in new compounds. *Nature Materials*. **16**, 964–967 (2017).

5. S. I. Seok, M. Grätzel, N.-G. Park, Methodologies toward Highly Efficient Perovskite Solar Cells. *Small*. **14**, 1704177 (2018).

6. Y. Yang, J. You, Make perovskite solar cells stable. *Nature*. **544**, 155–156 (2017).

7. J. A. Christians, P. A. Miranda Herrera, P. V. Kamat, Transformation of the excited state and photovoltaic efficiency of $CH_3NH_3PbI_3$ perovskite upon controlled exposure to humidified air. *Journal of the American Chemical Society*. **137**, 1530–1538 (2015).

8. B. Conings *et al.*, Intrinsic Thermal Instability of Methylammonium Lead Trihalide Perovskite. *Advanced Energy Materials*. **5** (2015), doi:10.1002/aenm.201500477.

9. G. E. Eperon *et al.*, Formamidinium lead trihalide: a broadly tunable perovskite for efficient planar heterojunction solar cells. *Energy & Environmental Science*. **7**, 982 (2014).

10. J. A. Christians, S. N. Habisreutinger, J. J. Berry, J. M. Luther, Stability in Perovskite Photovoltaics: A Paradigm for Newfangled Technologies. *ACS Energy Letters*. **3**, 2136–2143 (2018).

11. Y. Wang, T. Zhang, M. Kan, Y. Zhao, Bifunctional Stabilization of All-Inorganic α-$CsPbI_3$ Perovskite for 17% Efficiency Photovoltaics. *Journal of the American Chemical Society*. **140**, 12345–12348 (2018).

12. M. Kulbak, D. Cahen, G. Hodes, How Important Is the Organic Part of Lead Halide Perovskite Photovoltaic Cells? Efficient $CsPbBr_3$ Cells. *Journal of Physical Chemistry Letters*. **6**, 2452–2456 (2015).

13. J. Liang *et al.*, All-Inorganic Perovskite Solar Cells. *Journal of the American Chemical Society*. **138**, 15829–15832 (2016).

14. S. Dastidar *et al.*, Quantitative Phase-Change Thermodynamics and Metastability of Perovskite-Phase Cesium Lead Iodide. *J. Phys. Chem. Lett.* **8**, 1278–1282 (2017).

5. L. A. Frolova *et al.*, Highly efficient all-inorganic planar heterojunction perovskite solar cells produced by thermal coevaporation of CsI and PbI_2. *Journal of Physical Chemistry Letters*. **8**, 67–72 (2017).

16. A. Marronnier *et al.*, Anharmonicity and Disorder in the Black Phases of Cesium Lead Iodide Used for Stable Inorganic Perovskite Solar Cells. *ACS Nano*. **12**, 3477–3486 (2018).

8. T. Burwig, W. Fränzel, P. Pistor, Crystal Phases and Thermal Stability of Co-evaporated $CsPbX_3$ (X = I, Br) Thin Films. *The Journal of Physical Chemistry Letters*. **9**, 4808–4813 (2018).

18. D. Zhang *et al.*, Ultrathin Colloidal Cesium Lead Halide Perovskite Nanowires. *Journal of the American Chemical Society*. **138**, 13155–13158 (2016).

19. Y. Wang *et al.*, All-Inorganic Colloidal Perovskite Quantum Dots: A New Class of Lasing Materials with Favorable Characteristics. *Advanced Materials*. **27**, 7101–7108 (2015).

11. A. Swarnkar *et al.*, Quantum dot-induced phase stabilization of α-$CsPbI_3$ perovskite for high-efficiency photovoltaics. *Science*. **354**, 92–95 (2016).

12. B. Zhao *et al.*, Thermodynamically Stable Orthorhombic γ-$CsPbI_3$ Thin Films for High-Performance Photovoltaics. *Journal of the American Chemical Society*. **140**, 11716–11725 (2018).

22. Y. Fu *et al.*, Stabilization of the Metastable Lead Iodide Perovskite Phase via Surface Functionalization. *Nano Letters*. **17**, 4405–4414 (2017).

14. M. Lu *et al.*, Spontaneous Silver Doping and Surface Passivation of $CsPbI_3$ Perovskite Active Layer Enable Light-Emitting Devices with an External Quantum Efficiency of 11.2%. *ACS Energy Letters*. **3**, 1571–1577 (2018).

15. Y. Hu *et al.*, Bismuth Incorporation Stabilized α-$CsPbI_3$ for Fully Inorganic Perovskite Solar Cells. *ACS Energy Letters*. **2**, 2219–2227 (2017).

25. Z. Li *et al.*, Stabilizing Perovskite Structures by Tuning Tolerance Factor: Formation of Formamidinium and Cesium Lead Iodide Solid-State Alloys. *Chemistry of Materials*. **28**, 284–292 (2016).

26. K. M. Rabe, U. V. Waghmare, Strain coupling in perovskite structural transitions: A first principles approach. *Ferroelectrics*. **194**, 119–134 (1997).

27. F. He *et al.*, Structural phase transition in epitaxial perovskite films. *Physical Review B - Condensed Matter and Materials Physics*. **70**, 1–10 (2004).

28. G. E. Eperon *et al.*, Inorganic caesium lead iodide perovskite solar cells. *J. Mater. Chem. A*. **3**, 19688–19695 (2015).

29. Y. Cao *et al.*, Pressure-Tailored Band Gap Engineering and Structure Evolution of Cubic Cesium Lead Iodide Perovskite Nanocrystals. *The Journal of Physical Chemistry C*. **122**, 9332–9338 (2018).

30. R. E. Beal *et al.*, Cesium Lead Halide Perovskites with Improved Stability for Tandem Solar Cells. *The Journal of Physical Chemistry Letters*. **7**, 746–751 (2016).

31. D. M. Trots, S. V. Myagkota, High-temperature structural evolution of caesium and rubidium triiodoplumbates. *Journal of Physics and Chemistry of Solids*. **69**, 2520–2526 (2008).

23. R. J. Sutton *et al.*, Cubic or Orthorhombic? Revealing the Crystal Structure of Metastable Black-Phase $CsPbI_3$ by Theory and Experiment. *ACS Energy Letters*. **3**, 1787–1794 (2018).

33. V. Craciun, D. Craciun, X. Wang, T. J. Anderson, R. K. Singh, Transparent and Conducting Indium Tin Oxide Thin Films Grown by Pulsed Laser Deposition at Low Temperatures. *Journal of Optoelectronics and Advanced Materials*. **5**, 401–408 (2003).

34. Q. Shan *et al.*, High Performance Metal Halide Perovskite Light-Emitting Diode: From Material Design to Device Optimization. *Small*. **13**, 1701770 (2017).

ACKNOWLEDGEMENTS

Funding: The authors acknowledge financial support from the Research Foundation-Flanders (FWO, Grant Nos. G.0B39.15 and G098319N), the Research foundation- Flanders postdoctoral fellowship to J.A.S, C.M, H.Y, K.P.F.J, E.D, K.L, and S.M.J.R (grant numbers 12Y7218N, 12J1716N, 12R8718N, 12C2817N, 12O3719N, 12O0117N and 12T3519N respectively), the SB-FWO fellow shit to T.B (1SC1319), the KU Leuven Research Fund (C14/15/053), the Flemish government through long term structural funding Methusalem (CASAS2, Meth/15/04), the Hercules foundation (HER/11/14), and the Belgian Federal Science Policy Office (IAP-VII/05). The research leading to these results has received funding from the European Research Council under the European Union's Seventh Framework Programme (FP/2007-2013)/ERC Grant Agreement (Grant No. 307523 LIGHT). E.S is grateful for the GIWAXS experimental time performed at the NCD-SWEET beamline at ALBA synchrotron. T.B and V.V.S acknowledge the funding from the European Union's Horizon 2020 research and innovation program (consolidator ERC grant agreement No 647755 – DYNPOR (2015-2020)). V.V.S acknowledges the Research Board of Ghent University (BOF). The computational resources and services used were provided by Ghent University (Stevin Supercomputer Infrastructure) and the VSC (Flemish Supercomputer Center), funded by the Research Foundation - Flanders (FWO). **Author contributions:** J.A.S conceived the science, coordinated the research and wrote the manuscript, under the supervision of J.H and M.B.J.R. I.D, V.D, W.V, K.J, E.S and D.C assisted with the X-ray scattering experiments and analysis. H.J, H.Y, E.H.S and

E.D synthesised the materials under investigation, and C.M, Y.W, Y.D, D.M and Z.L prepared and characterized the LED devices. T.B performed the DFT calculations under supervision of S.M.J.R, K.L and V.V.S, with support from R.B.F. C.N and B.G performed the DSC experiments and M.S and H.T assisted in developing the science. All authors have approved the manuscript. **Competing interests:** The authors declare no competing financial interests. **Data and materials availability:** All data needed to evaluate the conclusions in this manuscript are present in the main text or the supplementary materials. Additional data or codes are available upon request to the corresponding authors.

SUPPLEMENTARY MATERIALS

Materials and Methods
Figs. S1 to S20
Tables S1 and S2
References (35 –41)